Noise analysis of grating-based x-ray differential phase contrast imaging

Vincent Revol, Christian Kottler, Rolf Kaufmann, Ulrich Straumann, and Claus Urban

---

Articles you may be interested in

Quantitative electron density characterization of soft tissue substitute plastic materials using grating-based x-ray phase-contrast imaging
Rev. Sci. Instrum. 85, 103708 (2014); 10.1063/1.4898052

Development of key devices of grating-based x-ray phase-contrast imaging technology at Shenzhen University
AIP Conf. Proc. 1466, 61 (2012); 10.1063/1.4742270

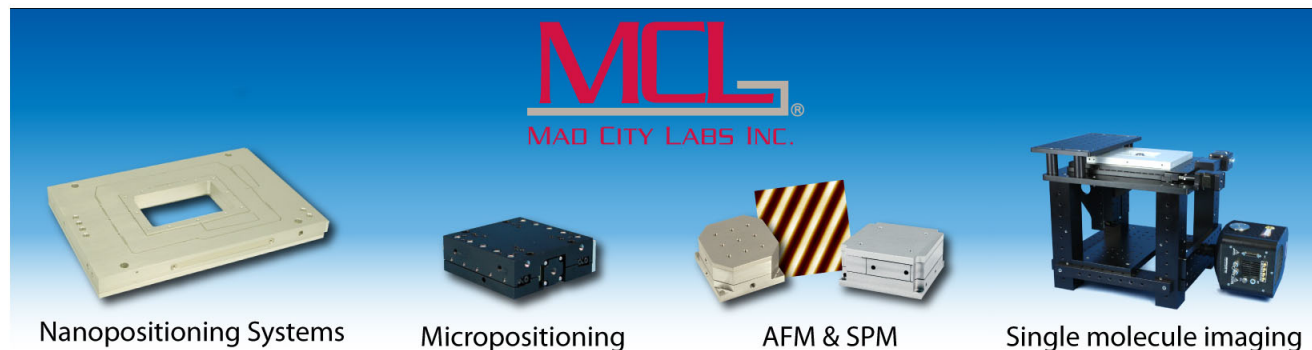Noise properties of grating-based x-ray phase contrast computed tomography
Med. Phys. 38, S106 (2011); 10.1118/1.3532396

Noise in x-ray grating-based phase-contrast imaging
Med. Phys. 38, 4133 (2011); 10.1118/1.3592935

Grating interferometer based scanning setup for hard x-ray phase contrast imaging
Rev. Sci. Instrum. 78, 043710 (2007); 10.1063/1.2723064

Noise analysis of grating-based x-ray differential phase contrast imaging

Vincent Revol,[1,a)] Christian Kottler,[1] Rolf Kaufmann,[1] Ulrich Straumann,[2] and Claus Urban[1]

[1]*Photonics Division, CSEM SA, 8005 Zürich, Switzerland*
[2]*Physics Institute, University of Zürich, 8057 Zürich, Switzerland*

The sensitivity of x-ray radiographic images, meaning the minimal detectable change in the thickness or in the index of refraction of a sample, is directly related to the uncertainty of the measurement method. In the following work, we report on the recent development of quantitative descriptions for the stochastic error of grating-based differential phase contrast imaging (DPCi). Our model includes the noise transfer characteristics of the x-ray detector and the jitter of the phase steps. We find that the noise in DPCi depends strongly on the phase stepping visibility and the sample properties. The results are supported by experimental evidence acquired with our new instrument with a field of view of 50×70 mm^2. Our conclusions provide general guidelines to optimize grating interferometers for specific applications and problems. © *2010 American Institute of Physics.* [doi:10.1063/1.3465334]

I. INTRODUCTION

X-ray imaging is an excellent and widely used tool to probe the internal structure of opaque objects. In fields as diverse as medicine, nondestructive testing, or security, it helps to diagnose, detect, or identify the sample without physical intrusion. Conventional radiographic systems, based on the absorption of x-rays in the sample, have however limited contrast for light materials such as plastics and biological tissues.

Techniques based on the phase shift of the x-ray beam induced by an object instead of its attenuation could provide a solution to this shortcoming. Indeed, in the energy domain of hard x-rays (10–100 keV), the real part of the index of refraction δ, responsible for the phase shift, is a factor of 100 to 1000 higher than its imaginary part β, responsible for the absorption. Furthermore, the dependence on the atomic number is weaker for δ than for β.[1] This implies that light elements overlapping with dense objects can be better visualized by using the phase shift as a contrast mechanism. Both facts potentially lead to an increase in the sensitivity of radiographic measurements and, consequently, in the field of applications of x-ray techniques.

Different methods have been developed to measure the phase shift of x-rays.[2–10] In our work, x-ray differential phase contrast imaging (DPCi),[11–15] based on a phase-sensitive grating interferometer, allows the detection of local changes in the direction of propagation of x-rays inside an object. Three images can be acquired simultaneously: the conventional transmission image T, the differential phase contrast image DP (based on the derivative of the phase shift of the x-ray beam in the sample), and the dark field image V,[16,17] which probes the submicroscopic inhomogeneities thanks to the measurement of the (ultra) small angle scattering (SAS)

power. DPCi has the following advantages over other techniques based on phase contrast: it can be used with standard large-focus x-ray tubes,[14] has a resolution in the order of tens of microns, and offers good absorption and phase sensitivity.[16] The instrument can also be used in a scanning system[18] or in computerized tomography.[19,20]

Though DPCi showed high potential in given situations, notably for soft-tissue[21] and organs imaging,[19] the ability to detect a given feature—for example, a void in an aluminum plate—strongly depends on the exact sample geometry and composition. As a result, this assessment commonly relies on a first experimental trial, which often ends in a loss of time and/or money. This underlines the need for a quantitative estimator of the stochastic error in DPCi images and, consequently, of the sensitivity of the method.

In the following sections, after a brief presentation of the grating interferometer method, we propose a model for the uncertainties present in the three images: T, DP, and V. This model includes the noise transfer characteristics of the scintillation-based x-ray detector and the mechanical jitter of the phase stepping stage, which are the two major noise contributions.

II. MATERIALS AND METHOD

A. Grating interferometer

DPCi with a grating interferometer has been studied extensively and is well documented in the literature.[11–15] It will, in the following, only be reviewed briefly. Figure 1(a) shows a schematic overview of the experimental setup. The instrument consists of a conventional x-ray tube (Comet MXR-160HP 20 with focal spot size of 1×1 mm^2), a complementary metal-oxide semiconductor-based x-ray detector (RadIcon Shad-o-Box 2k with 2048×1024 pixels of size 48×48 μm^2 and scintillator Min-R 2190)[22] and three x-ray
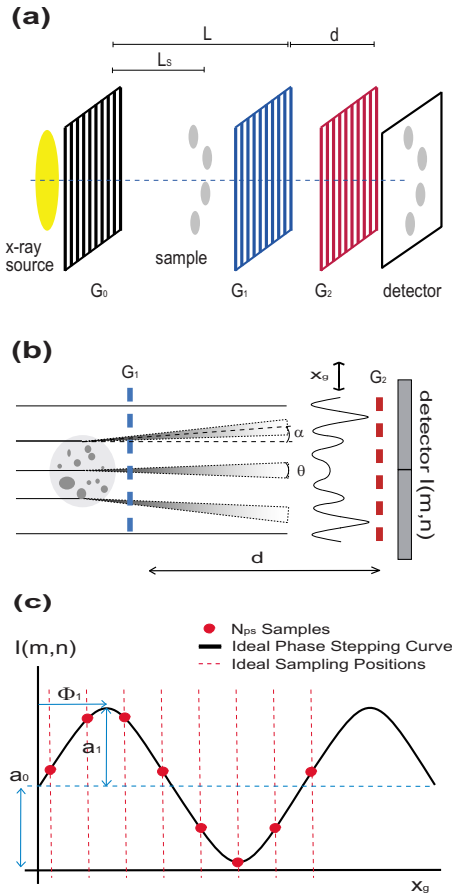
(a)

(b)

(c)

FIG. 1. (Color online) X-ray grating interferometer principle. (a) Setup with source grating G_0, beam-splitter grating G_1, and analyzer grating G_2. The distances are $L=131$ cm, between G_0 and G_1, $d=6.9$ cm, between G_1 and G_2, and $L_S \sim 126$ cm, between G_0 and the sample. (b) In the sample, the x-rays can be absorbed, deviated (angle α), or scattered (angular spread θ) as illustrated. This induces local changes in the interference fringes. (c) The phase stepping curve is the intensity $I(m,n)$ of a pixel (m,n) as a function of the position x_g of the interference pattern with respect to G_2. It is characterized by its average intensity a_0, its amplitude a_1, and phase ϕ_1.

gratings G_0, G_1, and G_2 with periodicities $p_0 = 57$ μm, $p_1 = 2.85$ μm, and $p_2 = 3$ μm and depths $H_0 = 60$ μm, $H_1 = 12.7$ μm, and $H_2 = 30$ μm, respectively.

The phase sensitive part consists of the beam-splitter grating G_1 and the analyzer grating G_2. G_1 [Fig. 1(a)] is a phase grating made out of silicon. The phase modulations induced by G_1 on the x-ray beam are transformed into intensity modulations on the plane of G_2 due to Fresnel diffraction[13] [Fig. 1(b)]. G_2 is an absorbing mask made out of gold with periodicity matching the one of the interference fringes. Thus, a change of the position of the intensity modulations with respect to G_2 locally induces a change of the intensity recorded by the corresponding pixel of the x-ray detector. By using the phase stepping method,[13,14,23] the lateral shift of the interference fringes due to the sample can be recovered as well as the conventional absorption image. Note that G_2 is only required since the periodicity of the interference fringes, in the order of some microns, is much smaller than the pixel size of conventional x-ray detectors, in the order of some tens of microns. Finally, the source grating G_0 is an absorbing mask made out of gold used to ensure a sufficient spatial coherence of the x-rays. It allows the use of
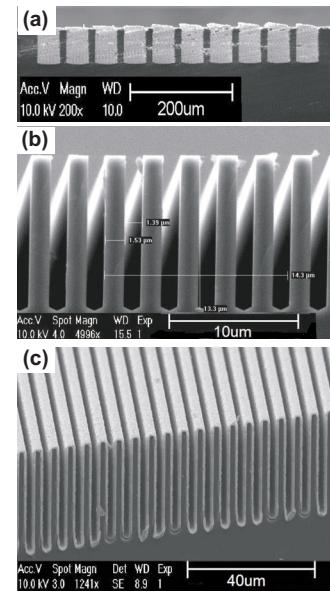

FIG. 2. (Color online) Cross sections obtained by scanning electron microscopy of (a) G_0 made by filling a silicon mold with gold, (b) G_1 made out of silicon, and (c) G_2 made by covering a silicon mold with a thin gold layer. The three gratings were produced in the clean rooms of CSEM in Neuchâtel.

conventional tube sources with a large focal spot.[14] The three gratings were optimized for an x-ray energy of 20 keV and produced on silicon wafers in the clean rooms of CSEM in Neuchâtel (CH) by a process involving photolithography, deep reactive ion etching, wet etching, and gold electroplating (Fig. 2).

B. Phase stepping and image extraction

The principle of the phase stepping method is the following. For each pixel (m,n) of the image, the pixel intensity $I(m,n,x_g)$ is recorded as a function of the position x_g of the interference pattern with respect to G_2 (see Fig. 1). The phase stepping curve thus results in an oscillating function with periodicity p_2. Its shape depends on the gratings' properties, alignment, sample characteristics, and energy spectrum.

In our particular setup, the phase stepping is done by a stepwise translation of G_0 in the direction perpendicular to the grating lines. Only a finite number of steps N_{ps} are acquired over one period p_2. The recorded intensity $I_k(m,n)$ for step $k = N x_g / p_2$ can then be written as a Fourier series

$$I_k(m,n) = \sum_i a_i(m,n)\sin\left[2\pi\frac{ik}{N_{ps}} + \phi_i(m,n)\right], \quad (1)$$

$$\sim a_0(m,n) + a_1(m,n)\sin\left[2\pi\frac{k}{N_{ps}} + \phi_1(m,n)\right], \quad (2)$$

where a_i are the amplitude coefficients and ϕ_i the phase coefficients.

Fundamentally, the idea to obtain images T, DP, and V is to compare the phase stepping curve $I_k^s(m,n)$, when a sample is present in the field of view, to a reference measurement $I_k^r(m,n)$ without an object, and thereby deduce the local changes in the beam propagation due to the object. In the

following, we will consistently use the superscripts (^{r}) and (^{s}) to refer to the reference and sample measurement, respectively.

For polychromatic x-ray spectra, $I_k(m,n)$ can be well approximated by a sine curve[16,17] and is then characterized by three coefficients: the mean intensity a_0, the amplitude a_1, and the phase ϕ_1 as defined in Eq. (2). The coefficients a_0, a_1, and ϕ_1 are extracted from the acquired data set $(I_k)_{k=1..N_{ps}}$[24] of the phase stepping curve by fast Fourier transform and are used to calculate three images as described below.

The image T is a measurement of the transmission of the sample as in conventional radiography. It is given by the relative change of the mean intensity a_0,

$$T(m,n) = \frac{a_o^s(m,n)}{a_o^r(m,n)}. \tag{3}$$

The differential phase contrast image DP can be obtained from the lateral shift of the intensity modulation, i.e., the change of the phase ϕ_1.[14]

$$DP(m,n) = \frac{\phi_1^s(m,n) - \phi_1^r(m,n)}{2\pi}. \tag{4}$$

A nonzero value implies that the x-rays were deviated in the direction perpendicular to the gratings' lines by an angle $\alpha(m,n) \sim p_2 DP(m,n)/d$ [see Fig. 1(b)]. α is proportional to the derivative of the phase shift in the sample[25] $\alpha(x) = (L_S\lambda/2\pi L)(\partial\varphi/\partial x)$, where $\varphi(x)$ is the phase shift of the x-rays wave front after propagation through the sample, L is the distance between G_0 and G_1, and L_S is the distance between G_0 and the object. Note that we normalized the phase difference by 2π, which is the maximal nonambiguous value that can be detected.

Finally, if we define the visibility of the phase stepping curve as $v^i(m,n) = a_1^i/a_0^i$ ($i = r$ or s), then the dark field image V is

$$V(m,n) = \frac{v^s(m,n)}{v^r(m,n)} = \frac{a_1^s(m,n)a_o^r(m,n)}{a_o^s(m,n)a_1^r(m,n)}. \tag{5}$$

It reflects the decrease of the visibility, which is essentially due to the local ultra-SAS power of the sample[16,17] [see Fig. 1(b)] and beam hardening, i.e., the shift of the x-ray spectrum toward higher energies due to the energy-dependent attenuation of the object.

As an example, Fig. 3 displays the experimental results for a felt-tip pen. For this experiment, the tube voltage was set to 40 kV. Under these conditions, the visibility was measured to be around 0.40. At each phase step, a raw image was acquired with a 1 min exposure time for a total of six phase steps. Accordingly, the total measurement time was around 12 min (including the reference measurement).

III. NOISE ANALYSIS

Let us consider the stochastic error of a single pixel and drop the indexes (m,n) for clarity. The measurement of T (DP and V) as defined by Eq. (3) [Eqs. (4) and (5)] is affected by various noise sources. Its statistical distribution will be characterized by the mean $\bar{T}$ ($\overline{DP}$ and $\bar{V}$) and the standard deviation σ_T (σ_{DP} and σ_V). Two major sources of
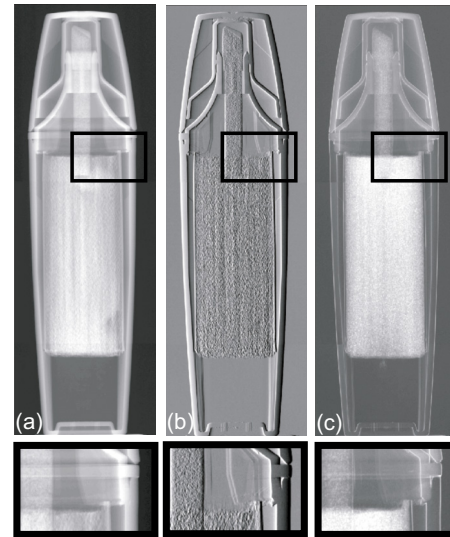

FIG. 3. (Color online) (a) Transmission T, (b) differential phase contrast DP, and (c) dark field V images obtained by DPCi for a felt-tip pen imaged at 40 kV (no filter) with six phase steps over one period. Bottom images are enlarged images from the inset. T probes the attenuation coefficient of the object while DP gives a measurement of the derivative in the direction perpendicular to the grating's lines of the phase shift of the x-ray beam. V reflects the local (ultra) SAS power of the sample that is, in this case, especially high in the highly structured ink tank.

uncertainties will be studied in detail, namely, the contributions $\sigma_{T,\text{det}}$ ($\sigma_{DP,\text{det}}$ and $\sigma_{V,\text{det}}$) from the detector noise at the digital output and $\sigma_{T,\text{jitter}}$ ($\sigma_{DP,\text{jitter}}$ and $\sigma_{V,\text{jitter}}$) from the phase stepping jitter in the sampled positions x_g. Other possible sources of errors $\sigma_{T,\text{other}}$ will finally be reviewed briefly. The total uncertainty of T (DP and V) will then be given by

$$\sigma_T^2 = \sigma_{T,\text{det}}^2 + \sigma_{T,\text{jitter}}^2 + \sigma_{T,\text{other}}^2. \tag{6}$$

A. Detector quantum noise

Our starting point is the measurement of the variance of the stochastic distribution of the digital output I of the x-ray detector as a function of the mean intensity. The latter was controlled by changing the anode current for a fixed tube voltage and exposure time. For this purpose, 100 successive exposures were recorded for each anode current. For each pixel, the mean and variance of the acquired intensity histogram were then estimated. Finally, the calculated means and variances were averaged over a 100×100 pixel area to obtain the average mean intensity $\bar{I}$ and average variance σ_I^2.

On Fig. 4, σ_I^2 is plotted as a function of $\bar{I}$ at 50 kV, once with 1.5 mm of silicon (equivalent to the beam hardening due to the three gratings) as filter and once with 1.5 mm of silicon and 5 mm aluminum as filter. The error bars show the standard deviation of σ_I^2 over the 100×100 pixel area which represents the pixel-to-pixel inhomogeneities of the detector.

Two conclusions can be drawn from this plot. First, the variance σ_I^2 is proportional to the mean intensity $\bar{I}$ over most of the dynamic range. The error due to the linear fit indeed stays below the level of the pixel-to-pixel inhomogeneities. Second, the slope of the linear fit with a 5 mm aluminum filter is higher than the one without. This increase is attributed to the beam hardening due to the aluminum plate and
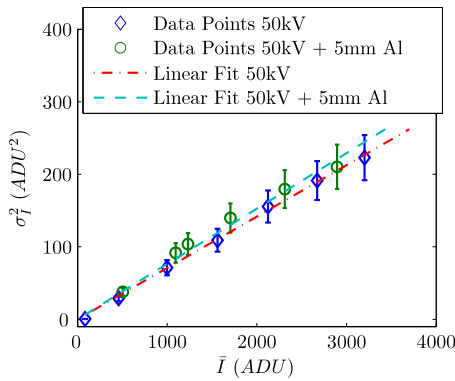
FIG. 4. (Color online) The variance σ_I^2 is plotted as a function of the mean output $\bar{I}$ for a tube voltage of 50 kV. The error bars represent the standard deviation of σ_I^2 due to the pixel-to-pixel inhomogeneities. In one case, 1.5 mm of silicon was used as filter (round markers) while on the other case, an additional 5 mm thick aluminum plate was added (square markers). In both cases, the data were fitted with a linear function (dashed and dotted-dashed lines). As they appear in the plot, the fitting coefficients depend on the energy spectrum of the incoming photons.

shows that the slope depends on the energy spectrum of the incoming photons. We can therefore assume that

$$\sigma_{I,\det}^2 = f_1 \bar{I}. \tag{7}$$

The slope f_1 is linked to the signal and noise transfer of the incoming x-ray photons to the output in arbitrary digital units (ADU). The reader is referred to the literature[26–28] for more details about this topic. Note that because of the beam hardening of the x-ray spectrum caused by the object, f_1 is in general different for the reference measurement f_1^r and for the sample measurement f_1^s.

The uncertainties of the acquired data set $\sigma_{I_k,\det}^i$ ($i=r$ or s) then translate into uncertainties of the images $\sigma_{T,\det}$, $\sigma_{DP,\det}$, and $\sigma_{V,\det}$ that can be calculated by using the error propagation formula[24,29] and the linear model of Eq. (7). It is assumed that N_{ps} is sufficiently high to prevent aliasing,[30]

which is reasonable for normal experimental conditions ($N_{ps} \geq 6$). The resulting expressions are summarized in Table I.

1. Background case

Let us consider first a situation where no object is in the field of view. In this case, the mean intensity a_0 and visibility v are equal for the reference and sample measurements. Furthermore there is no beam hardening. Therefore $\bar{T}=1$, $\bar{V}=1$, and $f_1^s=f_1^r=f_1$. The expressions for the relative uncertainty due to the detector quantum noise can then be simplified as displayed in Table I.

The results show that, for each image (T, DP, or V), the relative uncertainty decreases with the square root of the total integrated ADU during the phase stepping curve $I_{tot} = N_{ps}a_0$ and increases with the coefficient f_1. So the image quality improves if the mean intensity incoming on the detector goes up or if we use more phase steps. Moreover, for DP and V, the relative uncertainty decreases linearly with the visibility v. This underlines the importance of optimizing the latter to obtain a good sensitivity with DPCi.

2. General case

In the general case, the expressions are similar to the background case except for a multiplicative factor that depends on the absorption and visibility loss inside the object. This factor is at its minimum when $\bar{T}=1$ and $\bar{V}=1$, i.e., in the background case. As $\bar{T}$ becomes smaller, the relative uncertainty increases monotonically for each image (T, DP, or V). Qualitatively, the number of detected photons is lower when an object is present in the field of view and this degrades the quality of the images. However, note that $\sigma_T/\bar{T}$ is not sensitive to a loss of visibility while σ_{DP} and $\sigma_V/\bar{V}$ are.

At the limit, when the object is a strong absorber ($T \ll 1$) and when the visibility loss is large ($V \ll 1$), the contri-

TABLE I. Expressions for the contributions to the uncertainties in T, DP, and V from the detector quantum noise and the phase stepping jitter.

	General case	Background case
$\left(\dfrac{\sigma_{T,\det}}{\bar{T}}\right)^2 =$	$\dfrac{f_1^r}{N_{ps}a_0^r}\left(1+\dfrac{f_1^s}{\bar{T}f_1^r}\right)$	$\dfrac{2f_1^r}{N_{ps}a_0^r}$
$(\sigma_{DP,\det})^2 =$	$\dfrac{f_1^r}{2\pi^2 v^{r2} N_{ps}a_0^r}\left(1+\dfrac{f_1^s}{f_1^r \bar{T}\bar{V}^2}\right)$	$\dfrac{f_1^r}{\pi^2 v^{r2} N_{ps}a_0^r}$
$\left(\dfrac{\sigma_{V,\det}}{\bar{V}}\right)^2 =$	$\dfrac{f_1^r}{v^{r2} N_{ps}a_0^r}\left[v^{r2}\left(1+\dfrac{f_1^s}{f_1^r\bar{T}}\right)+2\left(1+\dfrac{f_1^s}{f_1^r\bar{T}\bar{V}^2}\right)\right]$	$\dfrac{2f_1^r}{v^{r2} N_{ps}a_0^r}(v^{r2}+2)$
$\left(\dfrac{\sigma_{T,\text{jitter}}}{\bar{T}}\right)^2 =$	$\dfrac{2\pi^2 v^{r2}}{N_{ps}}\left(\dfrac{\sigma_{x_g}}{p_2}\right)^2(1+\bar{V}^2)$	$\dfrac{4\pi^2 v^{r2}}{N_{ps}}\left(\dfrac{\sigma_{x_g}}{p_2}\right)^2$
$(\sigma_{DP,\text{jitter}})^2 =$	$\dfrac{3}{N_{ps}}\left(\dfrac{\sigma_{x_g}}{p_2}\right)^2$	$\dfrac{3}{N_{ps}}\left(\dfrac{\sigma_{x_g}}{p_2}\right)^2$
$\left(\dfrac{\sigma_{V,\text{jitter}}}{\bar{V}}\right)^2 =$	$\dfrac{2\pi^2}{N_{ps}}\left(\dfrac{\sigma_{x_g}}{p_2}\right)^2[2+v^{r2}(1+\bar{V}^2)]$	$\dfrac{4\pi^2}{N_{ps}}\left(\dfrac{\sigma_{x_g}}{p_2}\right)^2(1+v^{r2})$

butions from the phase stepping with sample (second term in the brackets) become dominant. The expressions then simplify and the relative uncertainties only depend on the characteristics of the sample phase stepping curve, i.e., the total integrated intensity $I_{tot}^s = T I_{tot}^r$, the visibility $v^s = V v^r$, and the conversion coefficient f_1^s.

B. Phase stepping jitter

The phase stepping is usually done by translating one of the three gratings. The actual position x_g (cf. Sec. II B and Fig. 1) is distributed around its ideal position due to mechanical uncertainties. This distribution is characterized by the standard deviation σ_{x_g} and translates into uncertainties in the sampled intensity value $I_k(m,n)$ and finally, in the images T, DP, and V. The error propagation formula can again be applied on Eq. (2) to obtain the contributions from the phase stepping jitter $\sigma_{T,\text{jitter}}$, $\sigma_{DP,\text{jitter}}$, and $\sigma_{V,\text{jitter}}$. The expressions are included in Table I.

The results show that the relative errors in images T, DP, and V due to the phase stepping jitter depend linearly on the relative error of the position with respect to the period of the phase stepping curve σ_{x_g}/p_2. For image T, the relative uncertainty is also proportional to v^r. Indeed, the smaller the visibility, the smaller is the error of the estimation of the average intensity a_0. On the contrary to T, the uncertainty of DP is independent of v^r.

C. Other noise sources

Though negligible in most cases, some other noise sources or nonidealities can also contribute to the degradation of the image quality for particular designs or conditions. On the one hand, the electronic noise of the detector and of the acquisition board induces an additional noise on the measured intensity I. It is called dark noise since it is not related to the illumination of the x-ray detector and can be measured by acquiring an image while the x-ray source is off. For our detector, it has been found (see Fig. 4) to be less than 1 ADU and is consequently ignored. On the other hand, fixed pattern noise due to the spatial nonuniformities of the gratings and/or of the detector as well as the mechanical drift of the gratings with respect to each other due to thermal instabilities can result in artifacts in the images. Practical solutions such as gain correction, optimized mechanical design, and temperature control can however be implemented to reduce these factors.

IV. RESULTS AND DISCUSSION

A set of experimental data has been collected to verify the expressions summarized in Table I. For a given set of gratings, phase stepping series were repeated at different anode currents, hence different photons flux for a constant tube voltage of 50 kV. Each phase stepping series (see Sec. II B) was done over one period of G_0 for a total of 12 phase steps and the exposure time was set to 6.7 s for each raw image. The field of view was divided in two parts: on one side, no object was present in the field of view while on the other side a 5mm thick aluminum plate (absorption $1-T=0.73$ and visibility loss $1-V=0.45$) was used to simulate a strongly ab-
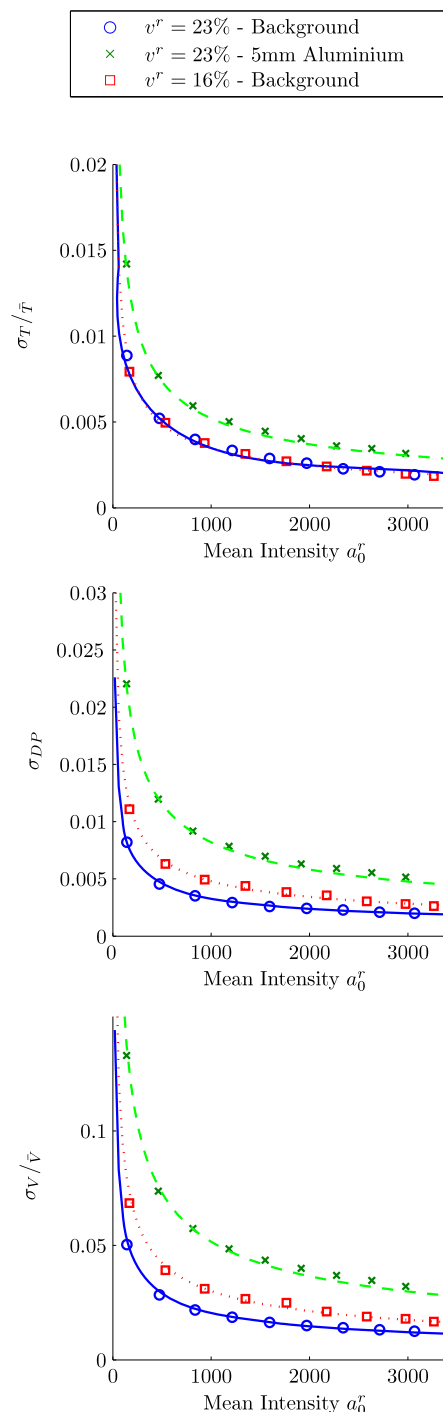

FIG. 5. (Color online) The relative uncertainties in (a) T, (b) DP, and (c) V were measured for a tube voltage of 50 kV as a function of the mean intensity a_0^r, in the background case with $v^r=0.23$ (round markers), in the background case with $v^r=0.16$ (square markers), and within the 5 mm aluminum plate ($T=0.27$ and $V=0.55$) with a visibility $v^r=0.23$ (cross markers). For each situation, the quantitative estimations of the model are indicated with solid lines (dotted line and dashed lines).

sorbing object. This procedure was repeated for two different G_0 gratings with duty cycle 0.3 and 0.5, for which the visibility v^r was 0.23 and 0.16, respectively.

For each situation, the average intensity a_0^r and the standard deviations σ_T, σ_{DP}, and σ_V were extracted from an area of 200×200 pixels. Figure 5 shows the measured uncertainties as a function of a_0^r as well as the predictions from the

theoretical model (see Table I). The conversion factors f_1^r =0.0709 and f_1^s=0.0764 used in the model estimations were extracted from the linear fit of the mean-variance plot at 50 kV (see Fig. 4). Moreover, the minimal incremental motion of the phase stepping stage is 0.3 μm,[31] which corresponds to a jitter on the phase stepping $\sigma_{x_g}/p_2 \sim 0.0017$.

Figure 5 shows a good agreement between the measurements and the theoretical model over the full dynamic range of the detector. As was discussed in the previous section, the relative uncertainties in T, DP, and V decrease as a function of the inverse square root of a_0^r and increase when an object is present in the field of view (here the 5 mm aluminum plate). Moreover, the relative uncertainty in T is independent of the decrease of v^r (different source gratings) while it increases for DP and V.

Note that under the present experimental conditions, the contributions from the detector quantum noise are dominant over the jitter noise. For example, for a visibility v^r=0.23 without object (background case), the relative uncertainty in T due to the jitter is around $\sigma_{T,\text{jitter}}/\bar{T}=0.67\times10^{-3}$, which is smaller than the contribution from the detector quantum noise $\sigma_{T,\text{det}}/\bar{T}>1.5\times10^{-3}$.

As an example, let us consider a void in a homogenous aluminum plate. Since the thickness measurement is affected by the uncertainties in T and DP, the void will only be identifiable if its dimension Δt is bigger than the standard deviation σ_t of the thickness measurement. σ_t is given for T and DP by

$$\sigma_{t,T} = \frac{1}{\mu_{Al}}\left(\frac{\sigma_T}{\bar{T}}\right), \tag{8}$$

$$\sigma_{t,DP} = \left(\frac{l_{\text{pixel}}p_1}{\delta_{Al}d}\right)\sigma_{DP}, \tag{9}$$

where the attenuation coefficient μ_{Al}=0.126 mm^{-1} and the real part of the index of refraction δ_{Al}=4.05$\times10^{-7}$ are taken at the mean energy E_{mean}=36.5 keV of the x-ray spectrum. d=6.9 cm is the distance between gratings G_1 and G_2, l_{pixel}=48 μm is the pixel size, and p_1=2.85 μm is the periodicity of G_1. Furthermore, the model shows that, for N_{ps}=12, v^r=0.23, and a_0^r=2500 ADU, the relative uncertainties behind a 5 mm thick aluminum plate are $\sigma_T/\bar{T}$=0.0033 and σ_{DP}=0.0052. This then corresponds to a minimal detectable thickness variation of Δt_T=26.2 μm and Δt_{DP}=25.4 μm per pixel using images T and DP, respectively.

Note that, even if δ and μ are related over the Kramers–Konig relation,[1] there is a fundamental difference in the imaging principles of T and DP. DP is indeed only sensitive to variations in the thickness or in the index of refraction while T is a direct measurement. So, in this particular example, a thickness variation of 100 μm distributed linearly over 10 pixels will be hardly seen in DP while it will be clear in T. On the other hand, DP is more sensitive to abrupt variations in the thickness or in the index of refraction than the absorption contrast.

V. SUMMARY

The main result of this work, presented in Table I, is the derivation of a theoretical model for the relative uncertainty levels in the three images T, DP, and V obtained with DPCi. The model includes the contributions from the detector noise transfer characteristics and the phase stepping jitter. It is supported by measurements done using our new instrument. It shows that, under normal operating conditions, the uncertainties are limited by the detector quantum noise.

The contributions from the detector noise are functions of the total integrated intensity during the phase stepping (number of phase steps times the average intensity), the visibility of the phase stepping curve, the noise transfer performances of the x-ray imaging system, and the absorption and visibility loss in the imaged sample. To improve the precision of a measurement, three approaches are thus available. First, the detective quantum efficiency of the x-ray detector could be increased. But the gain margin is thin since commercially available detectors are already strongly optimized. Another possibility is to use longer exposure times, more phase steps, or larger photon flux. However, since x-ray tubes have limited power, a trade-off has to be drawn between measurement time and sensitivity. Finally, the grating geometry and alignment can be optimized to obtain the best possible phase stepping visibility. Even though this requires large efforts in the microfabrication development of the gratings, the improvement potentially represents a decrease of a factor of 2 to 3 in the measurement uncertainty in comparison to what has been achieved previously. Significant improvement of the image quality with reasonably short exposure times could thus be realized using the last approach.

Finally, the principal outcome of these estimators is the ability to foresee if a feature within a given object can be potentially detected with DPCi and this, without experimental trial. The example of a void in an aluminum plate was evaluated above but the results are equally valid for most situations. With this tool, potential applications for which DPCi could be implemented can be targeted more efficiently.

ACKNOWLEDGMENTS

[1] J. Als-Nielsen and D. McMorrow, *Elements of Modern X-Ray Physics* (Wiley, Chichester, 2001).
[2] U. Bonse, Proc. SPIE **7078**, 707802 (2008).
[3] U. Bonse and M. Hart, Appl. Phys. Lett. **6**, 155 (1965).
[4] A. Momose, T. Takeda, Y. Itai, and K. Hirano, Nat. Med. **2**, 473 (1996).
[5] H.-C. Wang, H.-W. Peng, and M.-S. Kuo, Anal. Sci. **17**, 527 (2001).
[6] D. Chapman, W. Thomlinson, R. Johnston, D. Washburn, E. Pisano, N. Gmur, Z. Zhong, R. Menk, F. Arfelli, and D. Sayers, Phys. Med. Biol. **42**, 2015 (1997).
[7] M. Wernick, O. Wirjadi, D. Chapman, Z. Zhong, N. Galatsanos, Y. Yang, J. Brankov, O. Oltulu, M. Anastasio, and C. Muehleman, Phys. Med. Biol. **48**, 3875 (2003).
[8] K. A. Nugent, T. E. Gureyev, D. F. Cookson, D. Paganin, and Z. Barnea, Phys. Rev. Lett. **77**, 2961 (1996).
[9] P. Cloetens, W. Ludwig, J. Baruchel, J.-P. Guigay, P. Pernot-Rejmankova, M. Salome-Pateyron, M. Schlenker, J.-Y. Buffiere, E. Maire, and G. Peix, J. Phys. D: Appl. Phys. **32**, A145 (1999).

[10] A. Olivo and R. Speller, Phys. Med. Biol. **52**, 6555 (2007).

[11] C. David and T. Weitkamp, European Patent EP1731099A1 (2006).

[12] C. David and F. Pfeiffer, European Patent EP1879020A1 (2008).

[13] T. Weitkamp, A. Diaz, C. David, F. Pfeiffer, M. Stampanoni, P. Cloetens, and E. Ziegler, Opt. Express **13**, 6296 (2005).

[14] F. Pfeiffer, T. Weitkamp, O. Bunk, and C. David, Nat. Phys. **2**, 265 (2006).

[15] C. Kottler, C. David, F. Pfeiffer, and O. Bunk, Opt. Express **15**, 1175 (2007).

[16] F. Pfeiffer, M. Bech, O. Bunk, P. Kraft, E. Eikenberry, C. Brönnimann, C. Grünzweig, and C. David, Nature Mater. **7**, 134 (2008).

[17] F. Pfeiffer, M. Bech, O. Bunk, T. Donath, B. Henrich, P. Kraft, and C. David, J. Appl. Phys. **105**, 102006 (2009).

[18] C. Kottler, F. Pfeiffer, O. Bunk, C. Grünzweig, and C. David, Rev. Sci. Instrum. **78**, 043710 (2007).

[19] F. Pfeiffer, C. Kottler, O. Bunk, and C. David, Phys. Rev. Lett. **98**, 108105 (2007).

[20] Z.-T. Wang, K.-J. Kang, Z.-F. Huang, and Z.-Q. Chen, Appl. Phys. Lett. **95**, 094105 (2009).

[21] M. Bech, O. Bunk, C. David, R. Ruth, J. Rifkin, R. Loewen, R. Feiden-hans, and F. Pfeiffer, J. Synchrotron Radiat. **16**, 43 (2009).

[22] See http://www.rad-icon.com/ for the technical description of the x-ray detector.

[23] E. Wolf, Prog. Opt. **26**, 349 (1988).

[24] I. N. Bronshtein, K. A. Semendyayuv, G. Musiol, and H. Muehlig, *Handbook of Mathematics*, 4th ed. (Springer, Berlin, 2003).

[25] M. Born and E. Wolf, *Principles of Optics* (Pergamon, Oxford, 1980).

[26] H. J. Zweig, J. Opt. Soc. Am. **55**, 525 (1965).

[27] M. Rabbani, R. Shaw, and R. V. Metter, J. Opt. Soc. Am. A **4**, 895 (1987).

[28] I. A. Cunningham, M. S. Westmore, and A. Fenster, Med. Phys. **21**, 417 (1994).

[29] For a quantity Q that is a function of a set of random variables $(X_l)_{l=0..N-1}$, the standard deviation is given by $\sigma_Q^2 = \Sigma_{l=0,\ldots,N-1}(\partial Q/\partial X_l)^2 \sigma_{X_l}^2$. This result relies on the Taylor expansion of the function around its mean and assumes that the orders higher that the first one can be neglected.

[30] Aliasing refers to the distortion or artifact that results from the reconstruction of a continuous signal from a finite number of samples.

[31] See: http://www.newport.com/ for specifications of the linear stage Newport UTS series.